

Influences of a visco-elastically supported boundary on reflected waves in a couple-stress elastic half-space

C. D. WANG¹⁾, P. J. WEI¹⁾, P. ZHANG¹⁾, Y. Q. LI²⁾

¹⁾*Department of Applied Mechanics
University of Science and Technology Beijing
Beijing 100083, China
e-mail: weipj@ustb.edu.cn*

²⁾*Department of Mathematics
Qiqihar University
Qiqihar 161006, China*

THE REFLECTION OF ELASTIC WAVES at the surface of a couple-stress elastic half-space with a viscoelastic support is studied in this paper. Different from the classical elastic solid, there are: a non-dispersive dilatational propagating wave, a dispersive transverse propagating wave and a dispersive evanescent wave in a couple-stress elastic solid. The boundary conditions at the visco-elastically supported surface of a couple-stress elastic half-space include the couple-stress vector and the rotation vector, which disappear in the classical elastic solid. They are used to obtain a set of linear algebraic equation, from which the amplitude ratios of reflection waves with respect to the incident wave can be determined. Then, the reflection coefficients in terms of energy flux ratios are calculated numerically, and the normal energy flux conservation is used to validate the numerical results. At last, the influence of the boundary parameters that reflect the mechanical behavior of a viscoelastic support on the amplitude ratio, the phase shift and the energy partition of reflection waves are discussed based on the numerical results. Both the incident longitudinal displacement wave (the P-wave) and incident transverse displacement wave (the SV-wave) are considered. It is found that the instantaneous elasticity and the delayed viscosity of a viscoelastic support have different influences on the reflection waves.

Key words: reflection, viscoelastic support, couple-stress, dispersive waves, energy flux ratio.

Copyright © 2017 by IPPT PAN

1. Introduction

IN THE CLASSICAL ELASTIC THEORY, the stress at a material point is assumed to be dependent on the strain at the same material point, and no characteristic length is included in the constitutive relationships. Therefore, the classical elastic theory cannot describe the mechanical behavior of material at the micro- or nano-scale and capture/show the size effects observed experimentally [1]. In order to take into consideration the microstructure effects, the generalized continuum

theories, for example, the couple-stress theory [2, 3], the micromorphic theory [4], the micropolar theory [5], the microstretch theory [6] and the nonlocal theory [7] were proposed successively. In the problem of wave propagation, the classical elastic theory is also believed to be inadequate for a material with microstructure, and in particular, when the wavelength of an incident wave is comparable to the length of the material microstructure.

The couple-stress theory being one of the generalized continuum theories has received much attention. A couple-stress elastic solid differs from a classical elastic solid in that not only the force-stress but also the couple-stress can be maintained. A couple-stress elastic solid is also different from a micropolar elastic solid in that each mass point has not only the translational motion but also the dependent micro-rotational motion, while a micropolar elastic solid has an extra independent micro-rotational motion apart from the translational motion. TOUPIN [2], MINDLIN and TIERSTEN [3], KOITER [8] and others contributed to the establishment and development of the elastic theory of couple-stress solid. In the linear theory of couple-stress solid, there is an additional elastic modulus (called a bending-twisting modulus). The square root of the ratio of the bending-twisting modulus to the usual shear modulus has a dimension of length. The length l is an important material parameter that determines the differences between the couple-stress solid and the classical elastic solid. Usually, the length l is small in comparison with the dimension of a body and the wavelength normally encountered. However, its influences might become important as the dimension of a body or the wavelength diminish to the same order as the length l .

GRAFF and PAO [9] first studied the effects of couple-stress on the propagation of elastic wave in a couple-stress solid, and the reflection problem of elastic waves at free-surface of a couple-stress half-space and the propagation properties of a surface wave were also considered. It was found that the couple-stress solid could support three types of waves instead of two types as it is in a classical elastic solid and the two of them are dispersive. In the presence of couple-stress, the surface wave was found to propagate dispersively with the velocity that might be larger than the usual Rayleigh velocity. AGGARWAL and ALVERSON [10] further studied the diffraction of elastic waves by a cylindrical cavity or a rigid cylinder embedded in an infinite medium with couple-stress. OTTOSEN, RISTINMAA and LJUNG [11] studied Rayleigh waves in a linear elastic couple-stress medium. Their investigations showed that the Rayleigh wave turned out to be dispersive and the Rayleigh wave speed was always larger than the conventional Rayleigh wave speed. An explicit expression of the dispersion relation was also derived. GEORGIADIS and VELGAKI [12] also studied the dispersive properties of Rayleigh waves in a couple-stress solid. Their analysis showed that the Rayleigh wave propagating along the surface of a half-space was dispersive at high frequencies where the wavelength was of a micron order.

Provided that certain relationships held between various microstructure parameters in the theory employed, the dispersion curves of these waves had the same form as that given by the atomic lattice theory. The steady-state propagation of mode II and mode III crack in a couple-stress elastic material was also studied by GOURGIOTIS, MISHURIS, PICCOLROAZ and RADI [13, 14]. Their analysis confirmed and extended earlier results on the static case by including the effects of crack velocity and rotational inertia. KUMAR, KUMAR and NAUTIYAL [15] studied the propagation of shear waves in a couple-stress elastic half-space beneath an elastic layer. After developing the formal solution, a secular equation for surface wave propagation was derived. It was found that the frequency equations for different modes of propagation were dispersive in nature and the presence of rotation had significant effects on the dispersion curves. Considerable effect of elastic layer was also noticed on the dispersion curves. The dispersive properties of the torsional and surface SH-waves, and the reflection of body waves in an isotropic and homogenous elastic half-space characterized by dipolar gradient elasticity were studied by GOURGIOTIS, GEORGIADIS and NEOCLEOUS [16, 17].

In the above-mentioned studies, the interface between two different couple-stress solids or the other microstructured solids was usually assumed to be perfect, and the boundary surface was usually assumed to be free surface, namely, traction-free. However, the interface may be imperfect due to the interface accumulative damage, and the boundary surface may not be free but with various constraints in the actual engineering problems. The reflection of micropolar elastic waves at the non-free surface of a micropolar elastic half-space was studied by ZHANG, WEI and TANG [18]. The influences of the interface parameters on the reflection waves were discussed in detail. Furthermore, they also studied the reflection waves at the viscoelastically supported boundary of a micropolar half-space [19], and the reflective behavior of the pure elastic boundary, pure viscous boundary and the visco-elastic boundary were compared.

In this paper, the reflection problem of elastic waves at the visco-elastically supported boundary of a couple-stress half-space is studied. The visco-elastically supported boundary is modeled as a boundary with a distributed spring and dashpot. Each mass point at the boundary surface is subjected to the normal and tangent translational constraints and the rotational constraint. Three elastic boundary parameters and three viscous boundary parameters are introduced to represent the respective constraint degrees. The reflection waves are determined by the boundary condition with consideration of the force-stress, the couple-stress, the instantaneous elasticity, and the delayed viscosity. The influences of elastic and viscous boundary parameters on the amplitude ratio, the phase shift and the energy flux partition of reflection waves are discussed based on the numerical results.

2. Statements of problem

2.1. The elastic waves in the couple-stress solid

Different from the classical elastic solid, the couple-stress elastic solid can support not only the force-stress σ_{ij} but also the couple-stress μ_{ij} . Application of the conservation of the momentum and the moment of momentum to the representative volume element with the surface tractions $p_i = \sigma_{ij}n_j$ and the surface couples $m_i = \mu_{ij}n_j$ but without the body force and the body couples leads to

$$(2.1a) \quad \sigma_{ji,j} = \rho\ddot{u}_i,$$

$$(2.1b) \quad \mu_{ji,j} + e_{ijk}\sigma_{jk} = 0,$$

where e_{ijk} is the permutation symbol. Equations (2.1a) and (2.1b) can be combined to give

$$(2.2) \quad \sigma_{ji,j}^s - \frac{1}{2}e_{jik}\mu_{k,lj}^d = \rho\ddot{u}_i,$$

where σ_{ij}^s ($= \sigma_{ij} - \sigma_{ij}^a$) is the symmetrical part of σ_{ij} , μ_{ij}^d ($= \mu_{ij} - \frac{1}{3}\mu_{kk}\delta_{ij}$) is the deviatoric part of μ_{ij} in which δ_{ij} is the Kronecker delta. The constitutive relationships of the couple-stress solid are

$$(2.3a) \quad \sigma_{ij}^s = \lambda\varepsilon_{kk}\delta_{ij} + 2\mu\varepsilon_{ij},$$

$$(2.3b) \quad \mu_{ij}^d = 4\eta\chi_{ij} + 4\eta'\chi_{ji},$$

where λ and μ are the Lamé constants, and η and η' are the newly introduced material constants of the couple-stress solid. The strain tensor ε_{ij} and the curvature-twist tensor χ_{ij} are defined as

$$(2.4a) \quad \varepsilon_{ij} = \frac{1}{2}(u_{i,j} + u_{j,i}),$$

$$(2.4b) \quad \chi_{ij} = \omega_{j,i} = \frac{1}{2}e_{jkl}u_{l,ki},$$

where ω_i is the axial vector of strain tensor and u_i is the displacement vector. Inserting Eqs. (2.3) and (2.4) into Eq. (2.2) leads to the equation of motion of mass point in term of displacement components

$$(2.5) \quad (\lambda + \mu)u_{j,ji} + \mu u_{i,jj} + \eta(e_{ijk}e_{kmn}u_{n,mj}),_{ll} = \rho\ddot{u}_i.$$

It is noted that the material constant η' does not appear in the equation of motion. Furthermore, we represent u_i by introducing a scalar potential φ and a vector potential \mathbf{H} :

$$(2.6) \quad \mathbf{u} = \nabla\varphi + \nabla \times \mathbf{H} \quad (\nabla \cdot \mathbf{H} = 0).$$

Inserting Eq. (2.6) into Eq. (2.5) leads to

$$(2.7a) \quad (\lambda + 2\mu)(\nabla^2\varphi) - \rho\ddot{\varphi} = 0,$$

$$(2.7b) \quad \mu(1 - \eta/\mu\nabla^2)\nabla^2 H - \rho\ddot{H} = 0.$$

Equations (2.7a) and (2.7b) are the equations that the dilatational wave and shear wave in a couple-stress solid should satisfy.

We now consider only the plane strain problem, namely, the displacement field $u_z = 0$, while u_x and u_y are only the functions of (x, y) . Then, the vector potential is limited to $H = H_z e_z$, and Eq. (2.7) becomes

$$(2.8a) \quad c_1^2 \nabla^2 \varphi = \ddot{\varphi},$$

$$(2.8b) \quad c_2^2 (1 - l^2 \nabla^2) \nabla^2 H_z = \ddot{H}_z,$$

where $c_1^2 = (\lambda + 2\mu)/\rho$ and $c_2^2 = \mu/\rho$ are the phase speeds of dilatational wave and shear wave in the classical elastic solid, and $l = \sqrt{\eta/\mu}$ is a dimension of length and represents the effects of couple-stress embedded in the wave motion equation in a couple-stress solid. When $l = 0$, the couple-stress effects disappear and the wave motion equations, Eqs. (2.8a)–(2.8b), reduce to the ones for a classical elastic solid.

Let

$$(2.9a) \quad \varphi = f(y) \exp[i(\xi x - \omega t)],$$

$$(2.9b) \quad H_z = h(y) \exp[i(\zeta x - \omega t)].$$

Inserting Eq. (2.9) into Eq. (2.8) leads to

$$(2.10a) \quad f''(y) + \alpha^2 f(y) = 0,$$

$$(2.10b) \quad h_1''(y) + \beta^2 h_1(y) = 0,$$

$$(2.10c) \quad h_2''(y) - \gamma^2 h_2(y) = 0,$$

where

$$\alpha^2 = \alpha_1^2 - \xi^2, \quad \beta^2 = \beta_1^2 - \zeta^2, \quad \gamma^2 = \beta_2^2 + \zeta^2, \quad \alpha_1^2 = \omega^2/c_1^2, \\ \beta_1^2 = [-1 + (1 + 4l^2\omega^2/c_2^2)^{1/2}]/2l^2, \quad \beta_2^2 = [1 + (1 + 4l^2\omega^2/c_2^2)^{1/2}]/2l^2.$$

Thus, we obtain the solution of Eq. (2.8)

$$(2.11a) \quad \varphi = A_1 \exp[i(\xi x - \alpha y - \omega t)] + A_2 \exp[i(\xi x + \alpha y - \omega t)],$$

$$(2.11b) \quad H_{z1} = B_1 \exp[i(\zeta x - \beta y - \omega t)] + B_2 \exp[i(\zeta x + \beta y - \omega t)],$$

$$(2.11c) \quad H_{z2} = C_2 \exp[-\gamma y + i(\zeta x - \omega t)],$$

where Eq. (2.11a) shows that the dilatational wave in a couple-stress solid is a propagating wave and is non-dispersive. Its phase speed is the same as that of the dilatational wave in the classical elastic solid, namely, $c_p = c_1 = \sqrt{(\lambda + 2\mu)/\rho}$. In other words, the couple-stress effects do not influence the dilatational wave. Equation (2.11b) represents that one shear wave is a dispersively propagating wave with the phase speed of $c_s = c_2\sqrt{1 + l^2\beta_1^2(\omega, l)}$. Equation (2.11c) shows that the other shear wave is the surface wave of shear type and this wave exists only near the boundary or the interface. The surface wave is also a dispersive wave with the phase speed of $c_{ss} = \omega/\zeta$. It is noted that $c_s \rightarrow c_2$ as $\omega \rightarrow 0$ and $c_s \rightarrow \infty$ as $\omega \rightarrow \infty$. So the shear wave can propagate faster or slower than the dilatational wave. There is a critical angular frequency $\omega_c = c_1\sqrt{c_1^2 - c_2^2}/(lc_2)$, at which the shear wave has the same speed as the dilatational wave.

2.2. The boundary conditions and the amplitude ratios

Considering a half-space of couple-stress solid with visco-elastically supported boundary, the coordinate plane oxz is set as a boundary of the half-space and the positive y direction is set downward vertically, as shown in Fig. 1. The incident P-wave and SV-wave travel in the half-space with the incidence angles of θ_1 and θ_2 respectively, and impinge the surface of $y = 0$. We consider only the plane strain case, namely, $\mathbf{u} = (u_1, u_2, 0)$, $\mathbf{H} = (0, 0, H_z)$.

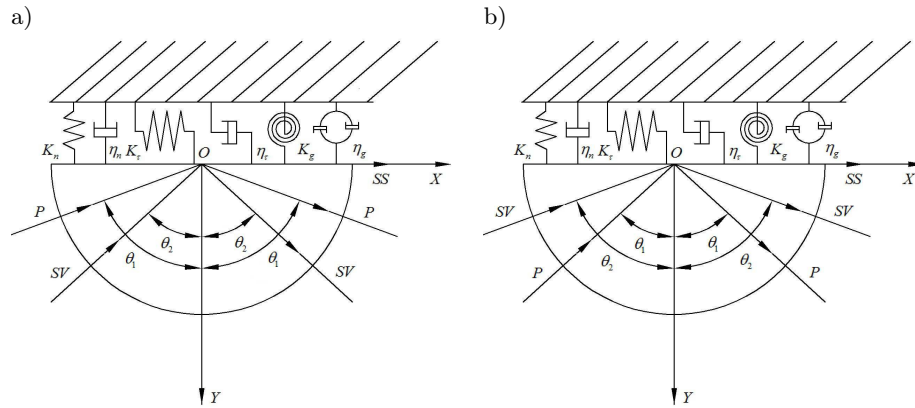


FIG. 1. Reflection waves at the boundary of a half-space of couple-stress solid with elastic and viscous support: a) $\omega < \omega_c$, b) $\omega > \omega_c$.

In the plane strain situation, the incident longitudinal wave (φ^I), the incident shear wave (H_{z1}^I), the reflection longitudinal wave (φ^R), the reflection shear wave

(H_{z1}^R) and the reflection surface wave of shear type (H_{z2}^R) can be expressed as

$$(2.12a) \quad \varphi^I = A_1 \exp[i(\xi x - \alpha y - \omega t)],$$

$$(2.12b) \quad H_{z1}^I = B_1 \exp[i(\zeta x - \beta y - \omega t)],$$

$$(2.12c) \quad \varphi^R = A_2 \exp[i(\xi x + \alpha y - \omega t)],$$

$$(2.12d) \quad H_{z1}^R = B_2 \exp[i(\zeta x + \beta y - \omega t)],$$

$$(2.12e) \quad H_{z2}^R = C_2 \exp[-\gamma y + i(\zeta x - \omega t)],$$

where A_1 , B_1 , A_2 , B_2 and C_2 are the amplitudes of various waves, respectively.

In order to establish the boundary condition, let us consider first the energy conservation in a representative volume element in absence of body force and body couple

$$(2.13) \quad \int_V [\frac{1}{2}\rho \dot{\mathbf{u}} \cdot \dot{\mathbf{u}} + W]_{t_0}^t dV = \int_{t_0}^t dt \int_S (\mathbf{n} \cdot \boldsymbol{\sigma} \cdot \dot{\mathbf{u}} + \mathbf{n} \cdot \boldsymbol{\mu} \cdot \dot{\boldsymbol{\omega}}) dS.$$

Let us consider that

$$(2.14) \quad \begin{aligned} \mathbf{n} \cdot \boldsymbol{\mu} \cdot \dot{\boldsymbol{\omega}} &= \mathbf{n} \cdot \boldsymbol{\mu} \cdot \mathbf{nn} \cdot \dot{\boldsymbol{\omega}} + \mathbf{n} \cdot \boldsymbol{\mu} \cdot (\mathbf{I} - \mathbf{nn}) \cdot \dot{\boldsymbol{\omega}} \\ &= \frac{1}{2}\mu_{nn} \mathbf{n} \cdot \nabla \times \dot{\mathbf{u}} + \mathbf{n} \cdot \boldsymbol{\mu} \cdot (\mathbf{I} - \mathbf{nn}) \cdot \dot{\boldsymbol{\omega}}, \end{aligned}$$

$$(2.15) \quad \frac{1}{2}\mu_{nn} \mathbf{n} \cdot \nabla \times \dot{\mathbf{u}} = \frac{1}{2}\mathbf{n} \cdot \nabla \times (\mu_{nn} \dot{\mathbf{u}}) - \frac{1}{2}\mathbf{n} \times \nabla \mu_{nn} \cdot \dot{\mathbf{u}},$$

and, if the surface S is smooth,

$$(2.16) \quad \int_S \mathbf{n} \cdot \nabla \times (\mu_{nn} \dot{\mathbf{u}}) dS = 0.$$

Equation (2.13) becomes

$$(2.17) \quad \begin{aligned} &\int_V [\frac{1}{2}\rho \dot{\mathbf{u}} \cdot \dot{\mathbf{u}} + W]_{t_0}^t dV \\ &= \int_{t_0}^t dt \int_S [(\mathbf{n} \cdot \boldsymbol{\sigma} - \frac{1}{2}\mathbf{n} \times \nabla \mu_{nn}) \cdot \dot{\mathbf{u}} + \mathbf{n} \cdot \boldsymbol{\mu} \cdot (\mathbf{I} - \mathbf{nn}) \cdot \dot{\boldsymbol{\omega}}] dS \\ &= \int_{t_0}^t dt \int_S [\mathbf{p} \cdot \dot{\mathbf{u}} + \mathbf{m} \cdot \dot{\boldsymbol{\omega}}] dS, \end{aligned}$$

where

$$(2.18) \quad \mathbf{p}_n = (\mathbf{n} \cdot \boldsymbol{\sigma} - \frac{1}{2} \mathbf{n} \times \nabla \mu_{nn}^d) = \mathbf{n} \cdot \boldsymbol{\sigma}^s + \frac{1}{2} \mathbf{n} \times (\nabla \cdot \boldsymbol{\mu}^d - \nabla \mu_{nn}^d),$$

$$(2.19) \quad \mathbf{m}_n = \mathbf{n} \cdot \boldsymbol{\mu} \cdot (\mathbf{I} - \mathbf{nn}).$$

Because the normal component of couple-tress vector on surface S enters in the combination with the force-stress vector as the coefficient of $\dot{\mathbf{u}}$. Only five boundary conditions rather than six are included in the couple-stress solid. The boundary values of three components of modified force-stress \mathbf{p}_n and the two tangent components of couple-stress \mathbf{m}_n are specified, or, alternatively, the boundary values of three components of displacement vector and two tangent components of rotational vector are specified. In the present situation, i.e., $\mathbf{n} = \mathbf{e}_y$, the modified force-stress can be expressed as

$$(2.20a) \quad p_{yx} = \sigma_{yx}^s + \frac{1}{2} \left(\frac{\partial \mu_{xz}^d}{\partial x} + \frac{\partial \mu_{yz}^d}{\partial y} \right),$$

$$(2.20b) \quad p_{yz} = \sigma_{yz}^s - \frac{1}{2} \left(\frac{\partial \mu_{xx}^d}{\partial x} + \frac{\partial \mu_{yx}^d}{\partial y} \right) + \frac{1}{2} \frac{\partial \mu_{yy}^d}{\partial x},$$

$$(2.20c) \quad p_{yy} = \sigma_{yy}^s,$$

$$(2.20d) \quad \mu_{yz} = 4\eta\omega_{z,y} + 4\eta'\omega_{y,z} = \eta\omega_{z,y}.$$

In the case of $\mathbf{n} = \mathbf{e}_x$, the modified force-stress can be expressed as

$$(2.20e) \quad p_{xy} = \sigma_{xy}^s - \frac{1}{2} \left(\frac{\partial \mu_{xz}^d}{\partial x} + \frac{\partial \mu_{yz}^d}{\partial y} \right),$$

$$(2.20f) \quad p_{xz} = \sigma_{xz}^s + \frac{1}{2} \left(\frac{\partial \mu_{xy}^d}{\partial x} + \frac{\partial \mu_{yy}^d}{\partial y} \right) - \frac{1}{2} \frac{\partial \mu_{xx}^d}{\partial y},$$

$$(2.20g) \quad p_{xx} = \sigma_{xx}^s,$$

$$(2.20h) \quad \mu_{xz} = 4\eta\omega_{z,x} + 4\eta'\omega_{x,z} = 4\eta\omega_{z,x}.$$

It is noted that the constitutive parameter η' does not work in the plane strain situation, but will play an important role in the anti-plane strain situation.

The visco-elastically supported boundary is modeled by the distributed spring and dashpot that are connected in parallel manner (Kelvin model). (K_n, K_τ, K_g) are the elastic constants of springs, while $(\eta_n, \eta_\tau, \eta_g)$ are the viscous constants of dashpots. The pure elastic support and the pure viscous support can be obtained easily. The boundary conditions for the pure elastic support can be expressed as

$$(2.21a) \quad p_{yy}|_{y=0} = K_n u_y|_{y=0},$$

$$(2.21b) \quad p_{yx}|_{y=0} = K_\tau u_x|_{y=0},$$

$$(2.21c) \quad \mu_{yz}|_{y=0} = K_g \omega_z|_{y=0},$$

The boundary condition for pure viscous support can be expressed as

$$(2.22a) \quad p_{yy}|_{y=0} = \eta_n \dot{u}_y|_{y=0},$$

$$(2.22b) \quad p_{yx}|_{y=0} = \eta_\tau \dot{u}_x|_{y=0},$$

$$(2.22c) \quad \mu_{yz}|_{y=0} = \eta_g \dot{\omega}_z|_{y=0},$$

The boundary conditions for viscoelastic support can be expressed as

$$(2.23a) \quad p_{yy}|_{y=0} = cK_n u_y|_{y=0} + (1-c)\eta_n \dot{u}_y|_{y=0},$$

$$(2.23b) \quad p_{yx}|_{y=0} = cK_\tau u_x|_{y=0} + (1-c)\eta_\tau \dot{u}_x|_{y=0},$$

$$(2.23c) \quad \mu_{yz}|_{y=0} = cK_g \omega_z|_{y=0} + (1-c)\eta_g \dot{\omega}_z|_{y=0},$$

where the index $c \in (0, 1)$ is the weigh factor. The elastically supported boundary and the viscously supported boundary can be recovered when $c \rightarrow 1$ or $c \rightarrow 0$, respectively.

The boundary conditions are applied to any point of coordinate x at any time t . This requires

$$(2.24) \quad \xi = \zeta,$$

namely, the apparent wavenumbers of dilatational wave and shear wave must be equal. This gives the relationship between the incidence angle and the reflection angle of the dilatational wave and the shear wave as follows:

$$(2.25) \quad \frac{\omega \sin \theta_1^I}{c_p} = \frac{\omega \sin \theta_2^I}{c_s(\omega, l)} = \frac{\omega \sin \theta_1^R}{c_p} = \frac{\omega \sin \theta_2^R}{c_s(\omega, l)} = \xi.$$

By using Eqs. (2.3), (2.4), (2.6) and (2.12), Eq. (2.23) leads to

$$(2.26a) \quad \mu(2\xi^2 - \omega^2/c_2^2)(A_1 + A_2) - 2\mu\zeta\beta(B_1 - B_2) + 2i\mu\gamma\zeta C_2 \\ = [cK_n + (1-c)\eta_n(-i\omega)][i\alpha(A_2 - A_1) - i\zeta(B_1 + B_2 + C_2)],$$

$$(2.26b) \quad 2\mu\xi\alpha(A_1 - A_2) + \mu(2\zeta^2 - \omega^2/c_2^2)(B_1 + B_2 + C_2) \\ = [cK_\tau + (1-c)\eta_\tau(-i\omega)][i\xi(A_1 + A_2) - i\beta(B_1 - B_2) - \gamma C_2],$$

$$(2.26c) \quad 2i\eta\beta\beta_1^2(B_2 - B_1) + 2\eta\gamma\beta_2^2 C_2 \\ = [cK_g + (1-c)\eta_g(-i\omega)][\frac{1}{2}\beta_1^2(B_1 + B_2) - \frac{1}{2}\beta_2^2 C_2].$$

Equation (2.26) can be rewritten in the form of matrix

$$(2.27) \quad (D_{ij})(A_2, B_2, C_2)^T = A_1\{e_i\} + B_1\{f_i\}.$$

The explicit expressions of D_{ij} , e_i and f_i corresponding to the visco-elastically supported boundary are given in the Appendix. The amplitude ratios of various

reflection waves can be obtained from Eq. (2.27). It should be pointed out that the amplitude ratios of reflection waves are dependent on the angular frequency of incident wave because both the reflection shear wave and surface wave are dispersive. This phenomenon is different from the classical elastic solid in which the amplitude ratios of reflection waves are not dependent on the angular frequency of incident wave.

2.3. Energy flux and energy flux conservation

Because the couple-stress solid can support not only the surface force but also the surface moment, the energy flux along the positive x and y axes can be calculated by

$$(2.28a) \quad I_x = -[\text{Re}(p_{xx}) \cdot \text{Re}(\dot{u}_x) + \text{Re}(p_{xy}) \cdot \text{Re}(\dot{u}_y) + \text{Re}(\mu_{xz}) \cdot \text{Re}(\dot{\omega}_z)],$$

$$(2.28b) \quad I_y = -[\text{Re}(p_{yx}) \cdot \text{Re}(\dot{u}_x) + \text{Re}(p_{yy}) \cdot \text{Re}(\dot{u}_y) + \text{Re}(\mu_{yz}) \cdot \text{Re}(\dot{\omega}_z)].$$

Thus, the energy flux along the propagation direction \mathbf{n} is

$$(2.29) \quad \mathbf{I}_n = I_x \mathbf{e}_x + I_y \mathbf{e}_y.$$

The average value of energy flux within a period is expressed as

$$(2.30) \quad \langle I_i \rangle = \frac{1}{T} \int_0^T I_i(t) dt = -\frac{1}{2} \text{Re}(p_{ij} \dot{u}_j^*) \quad (i = x, y).$$

The energy fluxes carried by the dilatational wave and the shear wave are respectively

$$(2.31a) \quad \langle I_x \rangle(\varphi) = -\frac{1}{2} \text{Re} \left[2\mu \frac{\partial^2 \varphi}{\partial x \partial y} \cdot \frac{\partial \dot{\varphi}^*}{\partial y} + \mu \left(k^2 \nabla^2 \varphi - 2 \frac{\partial^2 \varphi}{\partial y^2} \right) \cdot \frac{\partial \dot{\varphi}^*}{\partial x} \right],$$

$$(2.31b) \quad \langle I_y \rangle(\varphi) = -\frac{1}{2} \text{Re} \left[2\mu \frac{\partial^2 \varphi}{\partial x \partial y} \cdot \frac{\partial \dot{\varphi}^*}{\partial x} + \mu \left(k^2 \nabla^2 \varphi - 2 \frac{\partial^2 \varphi}{\partial x^2} \right) \cdot \frac{\partial \dot{\varphi}^*}{\partial y} \right],$$

$$(2.31c) \quad \langle I_x \rangle(H_z) = -\frac{1}{2} \text{Re} \left[-\mu \left(\frac{\partial^2 H_z}{\partial y^2} - \frac{\partial^2 H_z}{\partial x^2} + l^2 \nabla^4 H_z \right) \cdot \frac{\partial \dot{H}_z^*}{\partial x} \right. \\ \left. + 2\mu \frac{\partial^2 H_z}{\partial x \partial y} \cdot \frac{\partial \dot{H}_z^*}{\partial y} + \eta \frac{\partial(\nabla^2 H_z)}{\partial x} \cdot \nabla^2 \dot{H}_z^* \right],$$

$$(2.31d) \quad \langle I_y \rangle(H_z) = -\frac{1}{2} \text{Re} \left[\mu \left(\frac{\partial^2 H_z}{\partial y^2} - \frac{\partial^2 H_z}{\partial x^2} - l^2 \nabla^4 H_z \right) \cdot \frac{\partial \dot{H}_z^*}{\partial y} \right. \\ \left. + 2\mu \frac{\partial^2 H_z}{\partial x \partial y} \cdot \frac{\partial \dot{H}_z^*}{\partial x} + \eta \frac{\partial(\nabla^2 H_z)}{\partial y} \cdot \nabla^2 \dot{H}_z^* \right].$$

Inserting Eq. (2.12) into Eq. (2.31) leads to

$$\begin{aligned}
\langle I_x^I \rangle &= \frac{\xi\mu\omega^3}{2c_2^2}|A_1|^2 + \frac{1}{2}\zeta(\mu\omega^3/c_2^2 + \eta\beta_1^4\omega)|B_1|^2, \\
\langle I_y^I \rangle &= -\frac{\alpha\mu\omega^3}{2c_2^2}|A_1|^2 - \frac{1}{2}\beta(\mu\omega^3/c_2^2 + \eta\beta_1^4\omega)|B_1|^2, \\
\langle I_n^I \rangle &= \frac{\alpha_1\mu\omega^3}{2c_2^2}|A_1|^2 + \frac{1}{2}\beta_1(\mu\omega^3/c_2^2 + \eta\beta_1^4\omega)|B_1|^2, \\
\langle I_x^R \rangle(\varphi^R) &= \frac{\xi\mu\omega^3}{2c_2^2}|A_2|^2, & \langle I_y^R \rangle(\varphi^R) &= \frac{\alpha\mu\omega^3}{2c_2^2}|A_2|^2, \\
\langle I_n^R \rangle(\varphi^R) &= \frac{\alpha_1\mu\omega^3}{2c_2^2}|A_2|^2, \\
\langle I_x^R \rangle(H_{z1}^R) &= \frac{1}{2}\zeta(\mu\omega^3/c_2^2 + \eta\beta_1^4\omega)|B_2|^2, \\
\langle I_y^R \rangle(H_{z1}^R) &= \frac{1}{2}\beta(\mu\omega^3/c_2^2 + \eta\beta_1^4\omega)|B_2|^2, \\
\langle I_n^R \rangle(H_{z1}^R) &= \frac{1}{2}\beta_1(\mu\omega^3/c_2^2 + \eta\beta_1^4\omega)|B_2|^2,
\end{aligned}$$

for the incident P-wave, the incident SV-wave, the reflection P-wave, and the reflection SV-wave, respectively.

The surface wave always propagates along the surface, and the displacement distribution is not uniform at the wavefront. Therefore, the energy flux distribution is not uniform either. In fact, the energy flux density decreases gradually with an increase of y . Here, the unit area is taken to be $l_z \times l_y = \gamma \times 1/\gamma$ near the surface; then,

$$(2.32) \quad \langle I_x^R \rangle(H_{z2}^R) = \langle I_n^R \rangle(H_{z2}^R) = \frac{1 - e^{-2}}{4}\zeta\omega \left(4\gamma^2\mu + \eta\beta_2^4 + \mu\frac{\omega^2}{c_2^2} \right) |C_2|^2.$$

Let us define the energy flux ratios as

$$(2.33) \quad E_m = \frac{\langle I_n^R \rangle_m}{\langle I_n^I \rangle}, \quad (m = 1, 2, 3),$$

where $\langle I_n^I \rangle$ is the energy flux of incident wave and $\langle I_n^R \rangle_m$ ($m = 1, 2, 3$) is the energy flux of the reflection P-wave, the reflection SV-wave or the reflection SS-wave along the propagation direction. The energy conservation within a thin layer of boundary requires that the input energy flux is equal to the output energy flux, namely

$$(2.34) \quad E = (\langle I_y^R \rangle_1 + \langle I_y^R \rangle_2 + \langle I_y^R \rangle_3 + \langle I_t \rangle + \langle I_\eta \rangle) / \langle I_y^I \rangle = 1,$$

where

$$(2.35) \quad \langle I_t \rangle = \frac{1}{2} \operatorname{Re}(u_y K_n \dot{u}_y^* + u_x K_\tau \dot{u}_x^* + \omega_z K_g \dot{\omega}_z^*)$$

is the energy flux that enters the elastically supported boundary and $E_t = \langle I_t \rangle / \langle I_y^I \rangle$ stands for the energy flux ratios stored in the spring constraints. In fact, the average value of energy flux within a period in the spring constraint is null, namely, $\langle I_t \rangle = 0$. This implies that the spring constraints store and release energy periodically, but they do not absorb energy. Different from the spring constraint, the dashpot will definitely dissipate certain energy in a period. The energy dissipated in the viscous constraint boundary can be estimated by

$$(2.36) \quad \langle I_\eta \rangle = \frac{1}{2} \operatorname{Re}(\dot{u}_y \eta_n \dot{u}_y^* + \dot{u}_x \eta_\tau \dot{u}_x^* + \dot{\omega}_z \eta_g \dot{\omega}_z^*).$$

Equation (2.34) can be used to validate the numerical results in the next section.

3. Numerical results and discussions

In the numerical examples, the material constants of couple-stress elastic half-space are $\rho = 2.6 \times 10^3 \text{ kg/m}^3$, $\lambda = 2.2 \times 10^{10} \text{ N/m}^2$, $\mu = 1.1 \times 10^{10} \text{ N/m}^2$, and $\eta = 0.011 \text{ N}$. For the specified couple-stress solid, the critical circular frequency is $\omega_c = 7.1253 \times 10^9 \text{ rad/s}$, at which the reflection P-wave has the same propagation speed as that of the reflection SV-wave. Because the reflection SV-wave and the reflection surface wave (the SS-wave) are both dispersive, their reflection coefficients are not only dependent on the incident angle but also on the circular frequencies of incident wave. In order to investigate the difference between the elastic constraint boundary and the viscous constraint boundary, the amplitude ratios and the phase shifts of the reflection waves with respect to the incident waves are estimated for the elastic constraint boundary and the viscous constraint boundary, respectively. In the numerical calculation, the elastic and viscous benchmark parameters of the spring and the dashpot are assumed to be $K_n = 1 \times 10^{16} \text{ N/m}^3$, $K_\tau = 1 \times 10^{16} \text{ N/m}^3$, $K_g = 1 \times 10^4 \text{ N/m}$, $\eta_n = 1 \times 10^6 \text{ N}\cdot\text{s/m}^3$, $\eta_\tau = 1 \times 10^6 \text{ N}\cdot\text{s/m}^3$ and $\eta_g = 1 \times 10^{-6} \text{ N}\cdot\text{s/m}$. The actual parameters used in the numerical simulation are (cK_n, cK_τ, cK_g) and $(c\eta_n, c\eta_\tau, c\eta_g)$, where c is the scale coefficient indicating that the elastic parameters and the viscous parameters increase/decrease at the same proportion. In order to investigate the influences of elastic and viscous boundaries, the amplitude ratio, the phase shift and the energy partition of reflection waves are calculated in the present work for different incident angle and circular frequency in both cases of incident P-wave and incident SV-wave. The obtained numerical results are also validated by checking the energy conservation.

3.1. The case of incident P-wave

Figure 2 shows the amplitude ratios of reflection waves with respect to the incident wave in the case of elastically supported boundary. It is observed that the

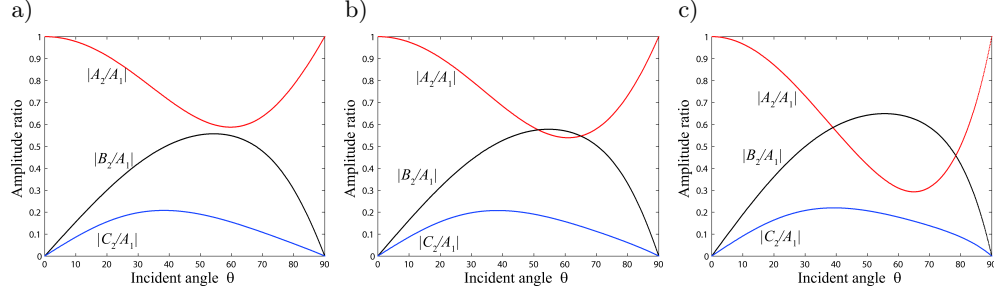


FIG. 2. Influences of elastic coefficients ($cK_n, cK_\tau, cK_g, \eta_n = \eta_r = \eta_g = 0$) on the amplitude ratios of reflection waves in the incident P-wave situation: a) $c = 0.5$, b) $c = 1$, c) $c = 2.5$.

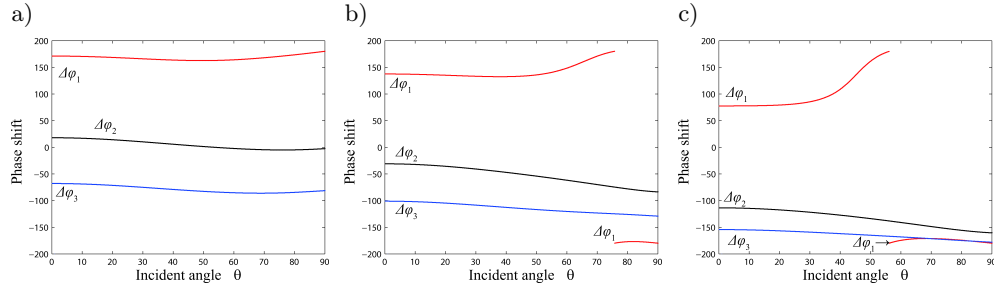


FIG. 3. Influences of elastic coefficients ($cK_n, cK_\tau, cK_g, \eta_n = \eta_r = \eta_g = 0$) on the phase shifts of reflection waves in the incident P-wave situation: a) $c = 0.5$, b) $c = 2.5$, c) $c = 8$.

amplitude of reflection P-wave decreases, while the amplitude of the reflection SV-wave and surface wave increase when the elastic constants of the constraint boundary increase gradually. This implies that the elastically supported boundary helps in the mode conversion. Figure 3 shows the phase shift of the reflection waves with respect to the incident wave. It is observed that the phase shift of reflection P-wave decreases, while the phase shift of reflection SV-wave and surface wave increase gradually as the elastic constants of constraint boundary increase gradually. In general, the elastically supported boundary affects not only the amplitude ratios but also the phase shifts. However, the influences on the reflection P-wave are opposite to the influences on the reflection SV-wave and the surface wave.

Figure 4 shows the energy flux ratios of reflection waves and the check on the energy conservation. Due to the dispersive nature, three kinds of incident angular frequencies are considered, namely, the critical frequency, the smaller frequency than the critical frequency and the greater frequency than the critical frequency. It is observed that the input energy flux converts gradually into

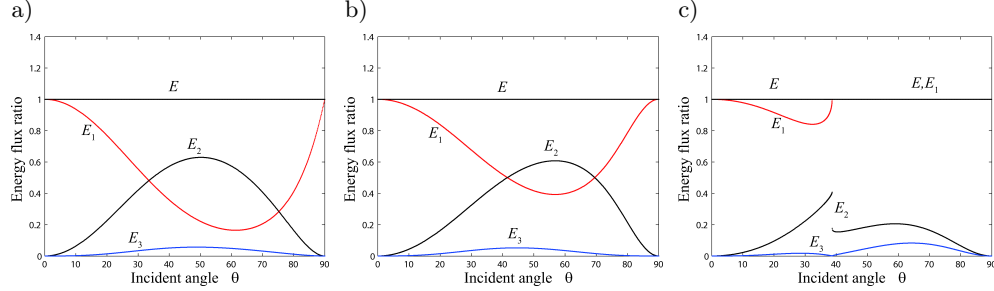


FIG. 4. Influences of incident frequency on the energy partition at elastic boundary ($K_n, K_\tau, K_g, \eta_n = \eta_\tau = \eta_g = 0$) in the incident P-wave situation: a) $\omega = 4 \times 10^9$ rad/s, b) $\omega = \omega_c = 7.1253 \times 10^9$ rad/s, c) $\omega = 2 \times 10^{10}$ rad/s.

the reflection P-wave as the incident frequency increases. When the incident frequency is greater than the critical frequency, the reflection SV-wave reaches its critical angle (about 38.6°) and the input energy flux converts into the reflection P-wave after the critical angle. Meanwhile, two surface waves propagate along the boundary surface with the energy flux along this surface too. The fact that the energy conservation index remains at nearly unity in total range of incident angle indicates that the energy flux conservation along the normal of boundary is satisfied as expected. The energy fluxes carried by various reflection waves exhibit the energy partition of the incident energy flux carried by the incident wave. The energy conservation validates the numerical results in the present work.

The free boundary and the fixed boundary were often discussed in the literature. In fact, these two kinds of boundaries are the two extreme cases of elastically supported boundary studied in this paper and can be both obtained from the present elastically supported boundary by assuming very small and very large constraint stiffness, respectively. Figure 5 shows the energy ratios of reflection waves obtained by the exact free boundary and the elastically supported boundary presented in this paper. It is observed that the numerical results obtained by the the elastically supported boundary are similar to the results obtained in the exact free boundary when very small values of the constraint stiffness are assumed. Figure 6 shows the energy ratios of reflection waves obtained by the exact fixed boundary and the studied elastically supported boundary. It is also observed that the numerical results obtained in the presented elastically supported boundary are similar to those obtained in the exact fixed boundary in which very large values of constraint stiffness are taken. All the above observations validate the numerical results in the present work.

Let us turn to the viscous constraint boundary. Figure 7 shows the influences of the viscous constants on the amplitude ratios of reflection waves. It is

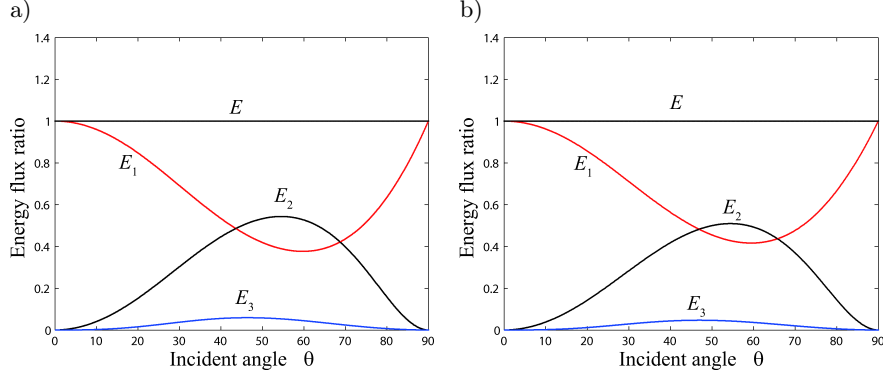


FIG. 5. Energy ratios for the free surface and the constrained surface with very small constraint stiffness in the incident P-wave situation ($\omega = 6 \times 10^9$ rad/s): a) free surface, b) constrained surface ($K_n = K_\tau = K_g = 10^4$, $\eta_n = \eta_\tau = \eta_g = 0$).

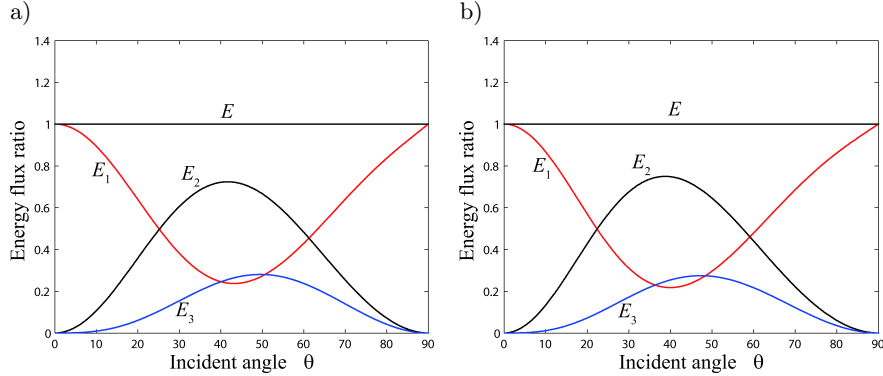


FIG. 6. Energy ratios for the fixed surface and the constrained surface with very large constraint stiffness in the incident P-wave situation ($\omega = 6 \times 10^9$ rad/s): a) fixed surface, b) constrained surface ($K_n = K_\tau = K_g = 0.4 \times 10^{18}$, $\eta_n = \eta_\tau = \eta_g = 0$).

observed that the amplitude of reflection P-wave decreases gradually, while the amplitudes of reflection SV-wave and the surface wave decrease first and then increase gradually when the viscous constants increase gradually. However, the amplitude ratio of reflection P-wave is at unity for the elastic boundary while it is evidently less than unity for the viscous boundary in the normal incident case. This phenomenon results from the delayed effects (between the response and the excitation) of the dashpot. The delayed effects make the dashpot different from the spring that has the instantaneous elasticity.

Figure 8 shows the influences of the viscous constants on the phase shifts of reflection waves in the viscous constraint boundary. It is noted that the phase

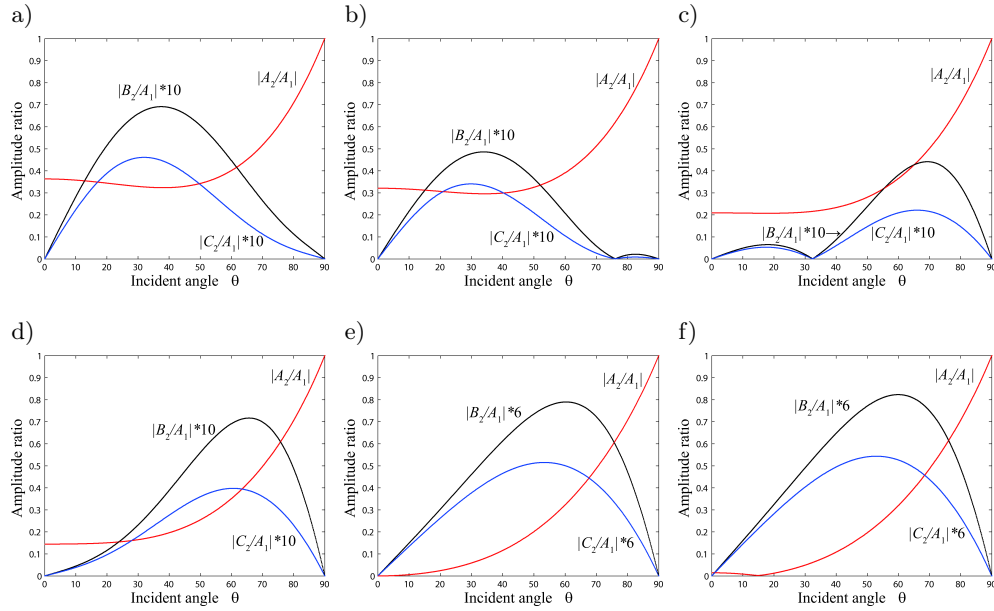


FIG. 7. Influences of the viscous coefficients ($K_n = K_\tau = K_g = 0$, $c\eta_n$, $c\eta_\tau$, $c\eta_g$) on the amplitude ratio of reflection waves in the incident P-wave situation ($\omega = 6 \times 10^9$ rad/s): a) $c = 5$, b) $c = 5.5$, c) $c = 7$, d) $c = 8$, e) $c = 10.7$, f) $c = 11$.

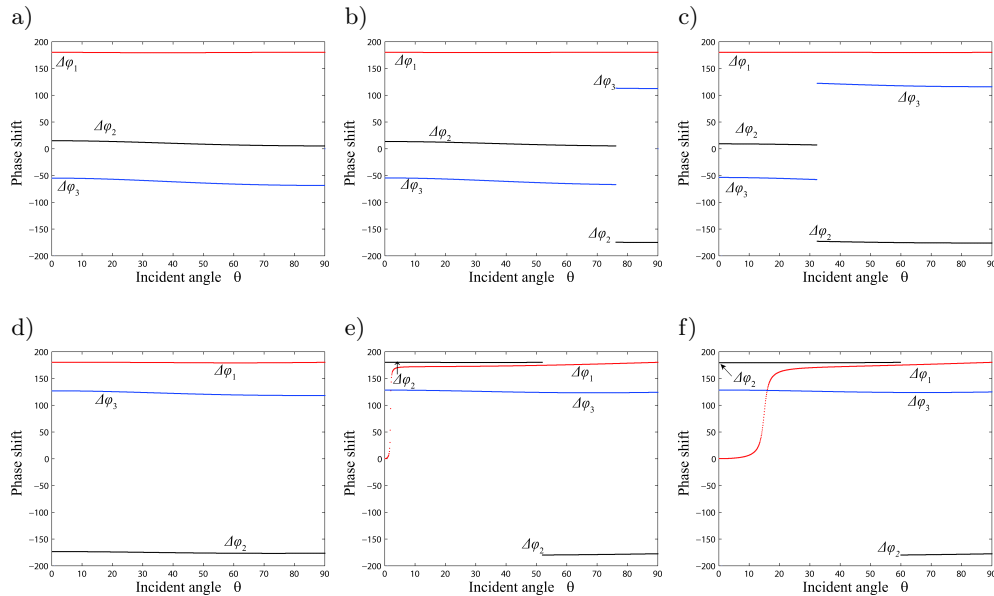


FIG. 8. Influences of viscous coefficients ($K_n = K_\tau = K_g = 0$, $c\eta_n$, $c\eta_\tau$, $c\eta_g$) on the phase shift in the incident P-wave situation ($\omega = 6 \times 10^9$ rad/s): a) $c = 5$, b) $c = 5.5$, c) $c = 7$, d) $c = 8$, e) $c = 10.7$, f) $c = 11$.

shift may undergo a sudden change when the viscous constants increase gradually. And the absolute value of a sudden change is always 180° (a sudden change of 360° is due to the principal value range of the anti-tangent function and does not mean the sudden change of the phase shift). Why is this? In order to explain this confusion, we tracked the change of the amplitude ratio. It was found that a sudden change of phase shift is always accompanied by the fact that the amplitude ratio becomes zero, see Figs. 7b and 7c. In other words, the complex amplitude ratio changes from one quadrant to the opposite quadrant (not an adjacent quadrant) across the initial point of complex plane and thus results in a sudden change of 180° of the phase shift. It was also noted that the sudden changes of the reflection SV-wave and surface wave take place at same time but earlier than the reflection P-wave. Compared with the elastic boundary, it is found that the phase shift changes suddenly for the viscous boundary (except the reflection P-wave), while it changes gradually in the elastic boundary. For the reflection P-wave, the phase shift changes both gradually and suddenly, namely, at certain incident angle, the phase shift takes a sudden change while it takes a gradual change at other incident angle.

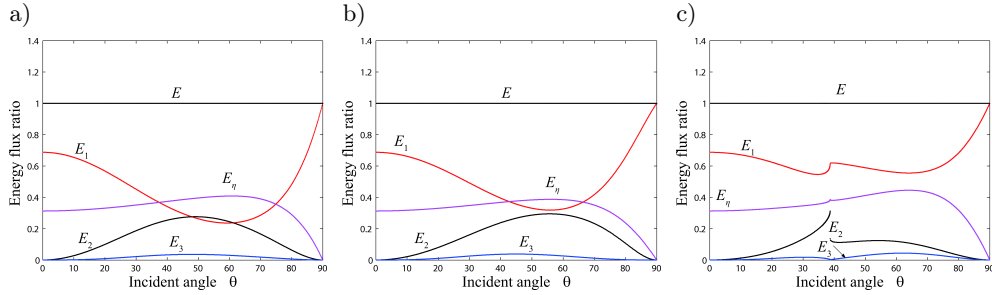


FIG. 9. Influences of incident frequency on the energy partition at viscous boundary ($K_n = K_\tau = K_g = 0$, $\eta_n, \eta_\tau, \eta_g$) in the incident P-wave situation: a) $\omega = 4 \times 10^9$ rad/s, b) $\omega = \omega_c = 7.1253 \times 10^9$ rad/s, c) $\omega = 2 \times 10^{10}$ rad/s.

Due to the dispersive nature, the reflection waves are dependent on the incident angular frequency. Figure 9 shows the energy fluxes carried by various reflection waves at different incident angular frequencies. Compared with the elastic boundary, the energy fluxes carried by various reflection waves decrease evidently in the case of viscous boundary. This can be explained by the fact that the viscous boundary dissipates certain energy while the elastic boundary does not dissipate any energy in one period. When the incident angular frequency increases, the energy flux carried by the reflection P-wave increases slightly, while the energy flux carried by the reflection SV-wave and surface wave produces unnoticeable change. The energy ratio dissipated by the viscous boundary with respect to the incident energy flux also produces unnoticeable change with the in-

creasing incident angular frequency. When the incident angular frequency is over the critical angle, the reflection SV-wave propagates faster than the reflection P-wave and reaches its critical angle early. Different from the elastic boundary case, the input energy flux does not concentrate completely on the reflection P-wave because a part of input energy is dissipated by the viscous boundary.

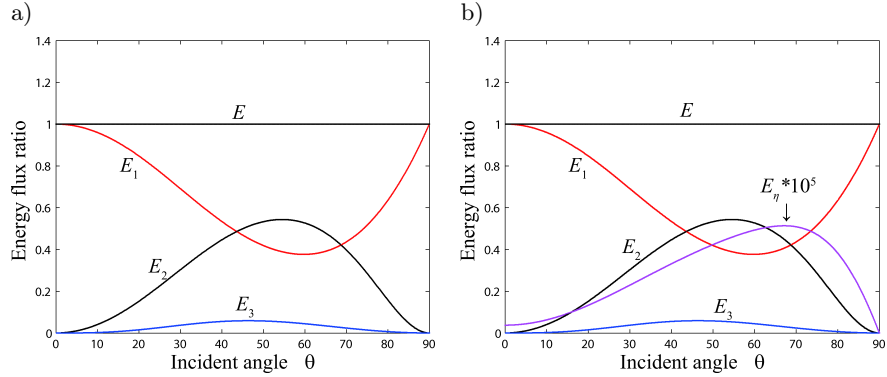


FIG. 10. Energy ratios for the free surface and the constrained surface with very small constraint stiffness in the incident P-wave situation ($\omega = 6 \times 10^9$ rad/s): a) free surface, b) constrained surface ($\eta_n = \eta_m = 10^0$, $\eta_g = 10^{-10}$, $K_n = K_\tau = K_g = 0$).

The free boundary and the fixed boundary can also be obtained from the viscous boundary under the study by assuming very small and very large viscous constants, respectively. Figure 10 shows the energy ratios of reflection waves obtained from the exact free boundary and the present viscous boundary with very small viscous constant. Figure 11 shows the energy ratios of reflection waves

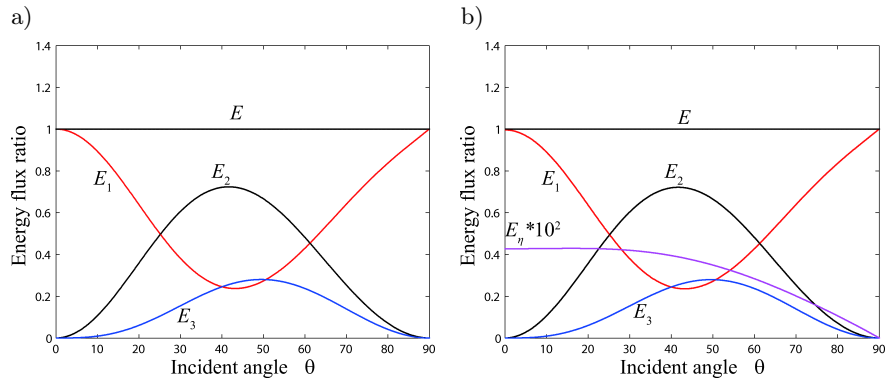


FIG. 11. Energy ratios for the fixed surface and the constrained surface with very large constraint stiffness in the incident P-wave situation ($\omega = 6 \times 10^9$ rad/s): a) fixed surface, b) constrained surface ($\eta_n = \eta_\tau = \eta_g = 10^{10}$, $K_n = K_\tau = K_g = 0$).

obtained from the exact fixed boundary and the present viscous boundary with very large viscous constant. The good consistency between the present viscous boundary and the free or fixed boundary validates the present numerical results.

3.2. The case of incident SV-wave

Figure 12 shows the influences of the elastic constraint stiffness on the amplitude of reflection waves for the elastic constraint boundary. Different from the incident P-wave case, the amplitude of the reflection P-wave increases first and then decreases gradually, while the amplitudes of the reflection SV-wave and the reflection surface wave decrease monotonously with the increasing elastic constraint stiffness. In the case of incident SV-wave with the incident angular frequency $\omega < \omega_{cr}$, the reflection P-wave reaches early its critical angle (about 68°). At the range of incident angle over critical angle, the amplitude ratio of reflection SV-wave always remains at unity.

Figure 13 shows the influences of the elastic constraint stiffness on the phase shift of reflection waves for the elastic constraint boundary. It is observed that the absolute value of the phase shift increases first and then decreases gradually with the increasing elastic constraint stiffness. However, the phase shift of the surface wave decreases monotonously with the increasing elastic constraint stiffness. Similar to the incident P-wave case, the phase shifts of reflection waves (except reflection surface wave) exhibit the characteristic of gradual change. Only after the critical angle, the reflection surface wave may have a sudden change.

Figure 14 shows the energy flux carried by various reflection waves at different incident angular frequencies. It is observed that the energy flux carried by the reflection P-wave decreases gradually, while the energy flux carried by reflection SV-wave increases gradually when the incident frequency increases. In other words, the input energy concentrates gradually on the reflection SV-wave in the incident SV-wave situation with the increasing incident angular frequency. The energy flux carried by the surface wave produces unnoticed change with the increasing incident angular frequency.

Figure 15 shows the influences of the viscous constraint coefficient on the amplitude of reflection waves for the viscous constraint boundary. Different from the incident P-wave case, the amplitude of the reflection SV-wave decreases, while the amplitude of reflection P-wave increases monotonously with the increasing viscous constraint coefficient. Figure 16 shows the influences of the viscous constraint coefficient on the phase shift of reflection waves for the viscous constraint boundary. It is observed that the phase shifts of reflection P-wave and reflection SS-wave change suddenly, the phase shifts of reflection SV-wave change both gradually and suddenly when the viscous coefficient increases. Compared with the incident P-wave situation, we may conclude that the phase shift of the reflec-

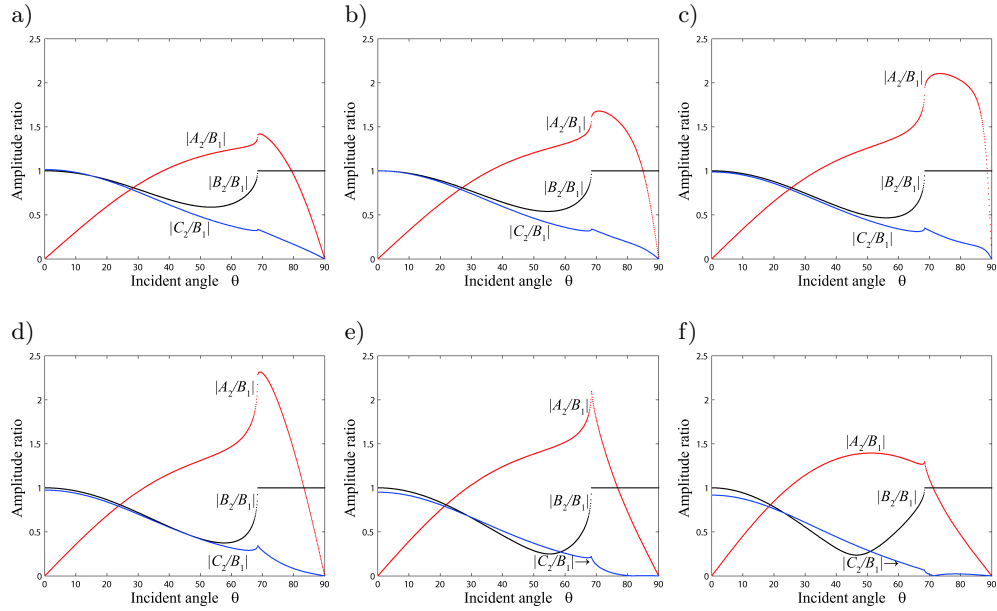


FIG. 12. Influences of elastic coefficient (cK_n , cK_τ , cK_g , $\eta_n = \eta_r = \eta_g = 0$) on the amplitude ratios of reflection waves in the incident SV-wave situation ($\omega = 6 \times 10^9$ rad/s): a) $c = 0.5$, b) $c = 1$, c) $c = 1.5$, d) $c = 2$, e) $c = 3$, f) $c = 5$.

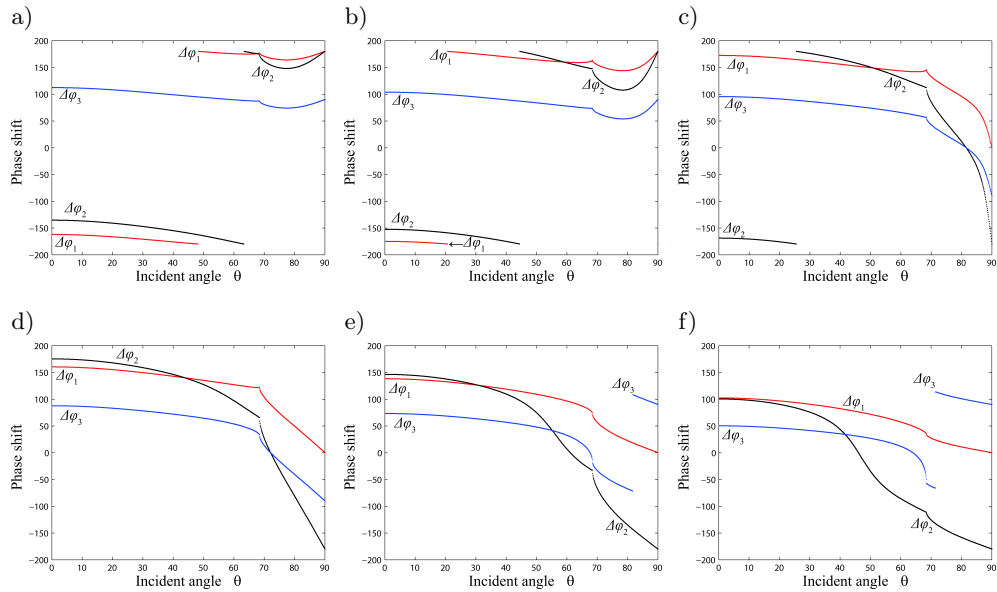


FIG. 13. Influences of elastic coefficients (cK_n , cK_τ , cK_g , $\eta_n = \eta_r = \eta_g = 0$) on the phase shifts of reflection waves in the incident SV-wave situation ($\omega = 6 \times 10^9$ rad/s): a) $c = 0.5$, b) $c = 1$, c) $c = 1.5$, d) $c = 2$, e) $c = 3$, f) $c = 5$.

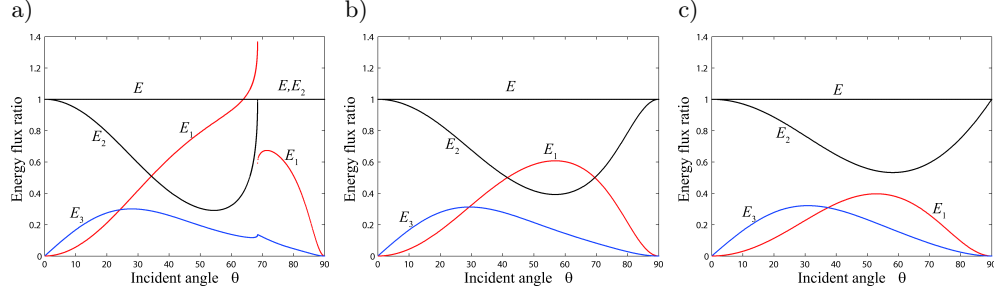


FIG. 14. Influences of incident frequency on the energy ratio at elastic boundary ($K_n, K_\tau, K_g, \eta_n = \eta_\tau = \eta_g = 0$) in the incident SV-wave situation: a) $\omega = 6 \times 10^9$ rad/s, b) $\omega = \omega_c = 7.1253 \times 10^9$ rad/s, c) $\omega = 9 \times 10^9$ rad/s.

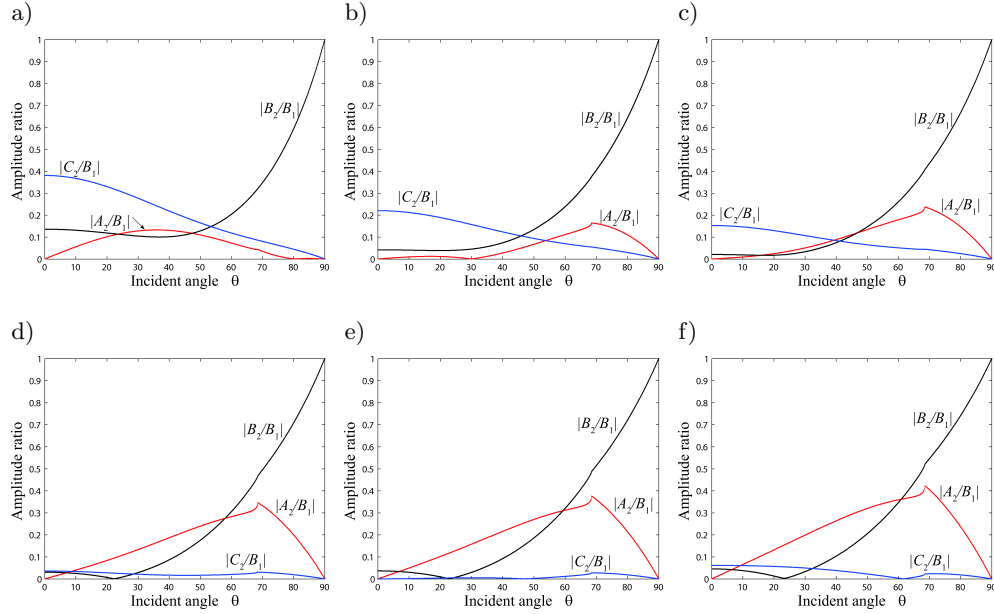


FIG. 15. Influences of viscous coefficients ($K_n = K_\tau = K_g = 0, c\eta_n, c\eta_\tau, c\eta_g$) on the amplitude ratios of reflection waves in the incident SV-wave situation ($\omega = 6 \times 10^9$ rad/s): a) $c = 5$, b) $c = 7$, c) $c = 8$, d) $c = 10$, e) $c = 10.7$, f) $c = 12$.

tion wave with the same type of the incident wave may change both gradually and suddenly, while it changes suddenly in the other two reflection waves.

Figure 17 shows the energy fluxes carried by various reflection waves at different incident angular frequencies. When the incident angular frequency increases, the energy flux carried by the reflection P-wave decreases gradually, while the en-

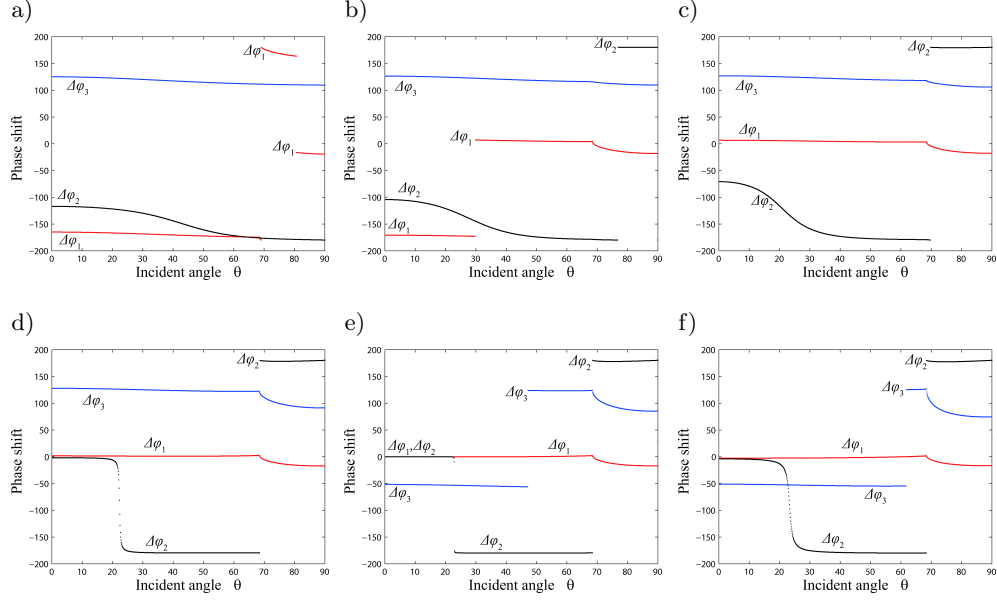


FIG. 16. Influences of viscous coefficients ($K_n = K_\tau = K_g = 0$, $c\eta_n$, $c\eta_\tau$, $c\eta_g$) on the phase shifts of reflection waves in the incident SV-wave situation ($\omega = 6 \times 10^9$ rad/s): a) $c = 5$, b) $c = 7$, c) $c = 8$, d) $c = 10$, e) $c = 10.7$, f) $c = 12$.

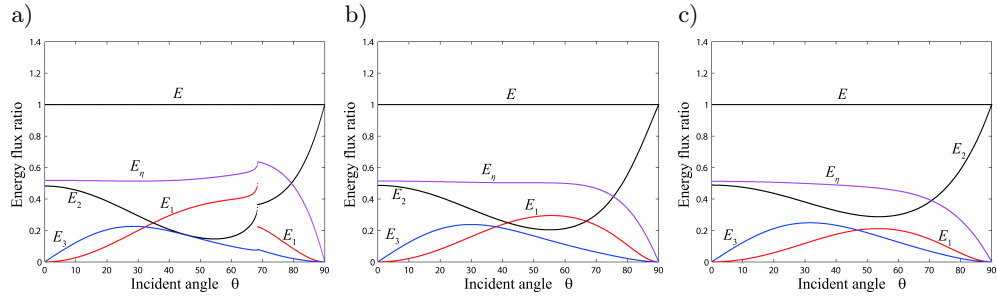


FIG. 17. Influences of incident frequency on the energy ratios at viscous boundary ($K_n = K_\tau = K_g = 0$, η_n , η_τ , η_g) in the incident SV-wave situation: a) $\omega = 6 \times 10^9$ rad/s, b) $\omega = \omega_c = 7.1253 \times 10^9$ rad/s, c) $\omega = 9 \times 10^9$ rad/s.

energy flux carried by the reflection SV-wave increases gradually. The energy flux carried by surface wave produces unnoticed change. The energy dissipated by the viscous boundary increases definitely when the incident angular frequency increases. But the energy flux ratio dissipated by the viscous boundary with respect to the incident energy flux also produces unnoticed change with the increasing incident angular frequency.

4. Conclusions

An elastic solid with couple-stress can support not only the force-stress but also the couple-stress. The boundary conditions include not only the displacement vector and the traction vector but also the rotation vector and the moment vector. The energy partition of various reflection waves is thus more complicated at the boundary of couple-stress solid than at the boundary of classical elastic solid. Usually, the free surface (without tractions and moments) and the fixed surface (without displacements and rotations) were taken into consideration in studies previously presented in the literature. In the present work, a visco-elastically constrained boundary is considered instead. The pure elastic boundary, the pure viscous boundary, the free boundary and the fixed boundary can be obtained from the present constrained boundary model. The amplitude ratios and the phase shifts of reflection waves are calculated for the pure elastic and pure viscous constrained boundary. Based on the numerical results, some conclusions can be drawn.

1) Compared with the free boundary, the elastic and viscous constraint boundaries help in the mode conversion. With an increase of the elastic or viscous constant, the reflection waves with the same type of the incident wave become weaker, while the reflection waves (except bulk wave or surface wave) with different types of the incident wave become stronger. In other words, the increasing elastic or viscous constants have same influences on the amplitude ratio of reflection waves.

2) The increase of elastic or viscous constant has different influences on the phase shifts of reflection waves. The phase shifts of reflection waves change in the way of gradual change when the elastic constants increase gradually. However, the phase shifts of reflection waves (except the reflection wave with same type of the incident wave) change in the way of sudden change of 180° when the viscous constants increase gradually. The reflection waves with the same type of the incident wave change in both ways of gradual change and sudden change when the viscous constants increase gradually.

3) The increase of elastic stiffness has evident different influences on the phase shift for incident P-wave and for incident SV-wave. In the case of incident P-wave, the phase shifts of reflection SV- and SS-waves increase gradually, while they decrease gradually for reflection P-wave. In the case of incident SV-wave, the absolute value of the phase shifts of reflection P- and SV-waves increases first and then decreases gradually with the increasing elastic stiffness. However, the phase shift of the surface wave decreases monotonously.

4) In the case of incident P-wave, the incident energy mainly concentrates on the reflection P-wave and the reflection SV-wave. The energy carried by the surface wave is smaller by one order of amplitude, at least. However, the energy

carried by the surface wave can be of the same order of amplitude as the reflection P-wave and SV-wave in the case of incident SV-wave.

5) Due to the dispersive nature of elastic waves in the couple-stress solids, the energy partition among various reflection waves may change with the change of incident angular frequency. When the incident angular frequency increases, the energy flux carried by the incident wave concentrates gradually on the reflection wave with the same type of incident wave, regardless whether the incident wave is P-wave or SV-wave and the constrained surface is elastic or viscous. Of course, the energy fluxes carried by the reflection waves for the viscous boundary are smaller than that for the elastic boundary because the viscous boundary dissipates a part of incident energy.

5. Acknowledgement

The work was supported by Fundamental Research Funds for the Central Universities (FRF-BR-15-026A), National Natural Science Foundation of China (No. 10972029), State science and technology support program (No. 2013BAK12B08), HeiLongJiang Natural Science Fund (No. B2015019).

Appendix

The explicit expressions of D_{ij} , e_i and f_i in Eq. (27) are

$$\begin{aligned}
D_{11} &= \mu(2\xi^2 - \omega^2/c_2^2) - icK_n\alpha - (1-c)\eta_m\omega\alpha, \\
D_{12} &= 2\mu\zeta\beta + icK_n\zeta + (1-c)\eta_m\omega\zeta, \\
D_{13} &= 2i\mu\gamma\zeta + icK_n\zeta + (1-c)\eta_m\omega\zeta, \\
D_{21} &= -2\mu\xi\alpha - icK_\tau\xi - (1-c)\eta_\tau\omega\xi, \\
D_{22} &= \mu(2\zeta^2 - \omega^2/c_2^2) - icK_\tau\beta - (1-c)\eta_\tau\omega\beta, \\
D_{23} &= \mu(2\zeta^2 - \omega^2/c_2^2) + cK_\tau\gamma - i(1-c)\eta_\tau\omega\gamma, \quad D_{31} = 0, \\
D_{32} &= 2i\eta\beta\beta_1^2 - \frac{1}{2}cK_g\beta_1^2 + \frac{1}{2}i(1-c)\eta_g\omega\beta_1^2, \\
D_{33} &= 2\eta\gamma\beta_2^2 + \frac{1}{2}cK_g\beta_2^2 - \frac{1}{2}i(1-c)\eta_g\omega\beta_2^2, \\
e_1 &= -\mu(2\xi^2 - \omega^2/c_2^2) - icK_n\alpha - (1-c)\eta_m\omega\alpha, \\
e_2 &= -2\mu\xi\alpha + icK_\tau\xi + (1-c)\eta_\tau\omega\xi, \quad e_3 = 0, \\
f_1 &= 2\mu\zeta\beta - icK_n\zeta - (1-c)\eta_m\omega\zeta, \\
f_2 &= -\mu(2\zeta^2 - \omega^2/c_2^2) - icK_\tau\beta - (1-c)\eta_\tau\omega\beta, \\
f_3 &= 2i\eta\beta\beta_1^2 + \frac{1}{2}cK_g\beta_1^2 - \frac{1}{2}i(1-c)\eta_g\omega\beta_1^2.
\end{aligned}$$

References

1. A.W. MCFARLAND, J.S. COLTON, *Role of material microstructure in plate stiffness with relevance to microcantilever sensors*, Journal of Micromechanics & Microengineering, **15**, 5, 1060–1067, 2005.
2. R.A. TOUPIN, *Elastic materials with couple-stresses*, Archive for Rational Mechanics and Analysis, **11**, 1, 385–414, 1962.
3. R.D. MINDLIN, H.F. TIERSTEN, *Effects of couple-stresses in linear elasticity*, Archive for Rational Mechanics and Analysis, **11**, 1, 415–448, 1962.
4. A.C. ERINGEN, *Mechanics of Micromorphic Materials*, Proceedings of the Eleventh International Congress of Applied Mechanics Munich (Germany), Springer, Berlin, 1966.
5. A.C. ERINGEN *Linear theory of micropolar elasticity*, Journal of Mathematics & Mechanics, **15**, 909–924, 1966.
6. A.C. ERINGEN, *Theory of thermo-microstretch elastic solids*, International Journal of Engineering Science, **28**, 12, 1291–1301, 1990.
7. A.C. ERINGEN, *Nonlocal Continuum Field Theories*, Springer, New York, 2001.
8. W.T. KOITER, *Couple-stresses in the theory of elasticity: I and II*, Nederlandse Akademie van Wetenschappen Proceedings Serie B, **67**, 17–44, 1964.
9. K.F. GRAFF, Y.H. PAO, *The effects of couple-stresses on the propagation and reflection of the plane waves in an elastic half-space*, Journal of Sound and Vibration, **6**, 2, 217–229, 1967.
10. H.R. AGGARWAL, R.C. ALVERSON, *The effect of couple-stresses on the diffraction of plane elastic waves by cylindrical discontinuities*, International Journal of Solids and Structures, **5**, 5, 491–511, 1969.
11. N.S. OTTOSEN, M. RISTINMAA, C. LJUNG, *Rayleigh waves obtained by the indeterminate couple-stress theory*, European Journal of Mechanics – A/Solids, **19**, 6, 929–947, 2000.
12. H.G. GEORGIADIS, E.G. VELGAKI, *High-frequency Rayleigh waves in materials with micro-structure and couple-stress effects*, International Journal of Solids and Structures, **40**, 10, 2501–2520, 2003.
13. G. MISHURIS, A. PICCOLROAZ, E. RADI, *Steady-state propagation of a Mode III crack in couple stress elastic materials*, International Journal of Engineering Science, **61**, 112–128, 2012.
14. P.A. GOURGIOTIS, A. PICCOLROAZ, *Steady-state propagation of a Mode II crack in couple stress elasticity*, International Journal of Fracture, **188**, 2, 119–145, 2014.
15. R. KUMAR, K. KUMAR, R. NAUTIYAL, *Propagation of SH-waves in couple stress elastic half space underlying an elastic layer*, Afrika Matematika, **24**, 4, 477–485, 2013.
16. P.A. GOURGIOTIS, H.G. GEORGIADIS, I. NEOCLEOUS, *On the reflection of waves in half-spaces of microstructured materials governed by dipolar gradient elasticity*, Wave Motion, **50**, 3, 437–455, 2013.
17. P.A. GOURGIOTIS, H.G. GEORGIADIS, *Torsional and SH surface waves in an isotropic and homogenous elastic half-space characterized by the Toupin–Mindlin gradient theory*, International Journal of Solids and Structures, **62**, 217–228, 2015.

18. P. ZHANG, P.J. WEI, Q.H. TANG, *Reflection of micropolar elastic waves at the non-free surface of a micropolar elastic half-space*, Acta Mechanica, **226**, 9, 2925–2937, 2015.
19. P. ZHANG, P.J. WEI, Y.Q. LI, *Reflection of longitudinal displacement wave at the viscoelastically supported boundary of micropolar half-space*, Meccanica, **52**, 7, 1641–1654, 2017.

Received September 8, 2016; revised version January 3, 2017.
